Monthly Notices
of the
ROYAL ASTRONOMICAL SOCIETY

MNRAS **501,** 347–355 (2021)
Advance Access publication 2020 November 21

doi:10.1093/mnras/staa3649

A survey of CH_2DOH towards starless and pre-stellar cores in the Taurus molecular cloud

Hannah E. Ambrose,★† Yancy L. Shirley★† and Samantha Scibelli

Steward Observatory, The University of Arizona, 933 N. Cherry Ave., Tucson, AZ 85721, USA

Accepted 2020 November 16. Received 2020 November 16; in original form 2020 June 12

ABSTRACT

Recent observations indicate that organic molecules are prevalent towards starless and pre-stellar cores. Deuteration of these molecules has not been well studied during the starless phase. Published observations of singly deuterated methanol, CH_2DOH, have only been observed in a couple of well-studied, dense, and evolved pre-stellar cores (e.g. L1544, L183). Since the formation of gas-phase methanol during this cold phase is believed to occur via desorption from the icy grain surfaces, observations of CH_2DOH may be useful as a probe of the deuterium fraction in the ice mantles of dust grains. We present a systematic survey of CH_2DOH towards 12 starless and pre-stellar cores in the B10 region of the Taurus molecular cloud. Nine of the 12 cores are detected with $[CH_2DOH]/[CH_3OH]$ ranging from <0.04 to $0.23^{+0.12}_{-0.06}$ with a median value of 0.11. Sources not detected tend to have larger virial parameters and larger methanol linewidths than detected sources. The results of this survey indicate that deuterium fractionation of organic molecules, such as methanol, during the starless phase may be more easily detectable than previously thought.

Key words: astrochemistry – stars: formation – ISM: clouds – ISM: individual objects: B10.

1 INTRODUCTION

Starless cores are dense ($>10^4$ cm^{-3}) clumps of gas and dust, typically with temperatures ∼10 K (Benson & Myers 1989; Bergin & Tafalla 2007; di Francesco et al. 2007). When a starless core becomes gravitationally bound, it enters the stage of star formation immediately prior to the formation of a protostar called a pre-stellar core (André et al. 2014). Most pre-stellar cores are low mass and coalesce into stars of a few solar masses or less. Starless and especially pre-stellar cores are relatively calm, non-turbulent environments that lack disruptive features such as internal heat sources, strong shocks and outflows, and strong temperature gradients. (Evans et al. 2001, Tafalla 2016). Therefore, they are a useful location to study the initial chemical conditions of star formation and ultimately, planet formation.

In the past decade, observations have shown that complex organic molecules (molecules with more than five atoms containing C, H, and either N or O; Herbst & van Dishoeck 2009) are detectable towards pre-stellar cores (e.g. Bacmann et al. 2012, Jiménez-Serra et al. 2016, Soma et al. 2018, Scibelli & Shirley 2020). A recent survey of 31 starless and pre-stellar cores in the L1495–B218 regions of Taurus showed methanol (100 per cent detection rate) and acetaldehyde (70 per cent detection rate) to be extremely common in starless and pre-stellar cores (Scibelli & Shirley 2020). Given the typical phase lifetimes of starless cores with densities of 10^5 cm^{-3} (André et al. 2014), these results indicate complex organic molecule formation is occurring at least hundreds of thousands of years prior to the formation of a protostar.

The deuteration of the complex organic molecules – the replacement of one or more hydrogen atoms with deuterium – is one aspect of complex organic molecule chemistry that has not been well studied to date during the starless core phase. Deuterated COMs are readily observed during low-mass protostellar phases (Loinard et al. 2002; Parise et al. 2002, 2006; Bianchi et al. 2017b; Jørgensen et al. 2018; Manigand et al. 2019; Taquet et al. 2019; Manigand et al. 2020; van Gelder et al. 2020) but there are few observations towards pre-stellar cores (cf. Bizzocchi et al. 2014; Chacón-Tanarro et al. 2019). Deuterium is primarily formed in the first few minutes of the big bang (Epstein, Lattimer & Schramm 1976) and is later incorporated into ^{3}He and heavier elements within stellar interiors. While the elemental D/H ratio is $\sim 2.6 \times 10^{-5}$, (Cooke et al. 2016; Planck Collaboration XIII 2016), in cold, dense environments such as starless and pre-stellar cores, molecular deuteration ratios can reach values several orders of magnitude above the cosmic abundance (Ceccarelli et al. 2014).

The fractionation of many commonly observed deuterated molecules (i.e. DCO^+, N_2D^+, NH_2D, etc.) is thought to proceed through gas phase reactions with H_2D^+, D_2H^+, and D_3^+ (Millar, Bennett & Herbst 1989; Roberts, Herbst & Millar 2003; Caselli, Sipilä & Harju 2019). For instance, NH_3 can react with H_2D^+ to form the intermediate ion NH_3D^+ that then can dissociatively recombine with an electron into NH_2D or NH_3 (with a branching ratio). This mechanism is unlikely to work for CH_3OH because the reaction of $CH_3OH_2^+ + e^-$ has been measured in the laboratory and dissociatively recombines into CH_3OH only a small fraction of the time (Geppert et al. 2006). Presumably, the same result is true for the deuterated ion $CH_2DOH_2^+$. Thus, significant gas phase

★ E-mail: heha2455@email.arizona.edu (HEA); yshirley@email.arizona.edu (YLS)
† Senior Honors Thesis at the University of Arizona

deuterium fractionation of methanol in cold (∼10 K) environments appears unlikely.

CH_2DOH is a strong candidate for the study of fractionation on the icy surfaces of dust grains. Models suggest that at least some methanol fractionation is occurring within grain ices, as the gas phase abundance of methanol cannot be explained by pure gas phase ion–molecule chemistry (Geppert et al. 2006, shown experimentally). Instead, CH_3OH is thought to form on the icy surfaces of dust grains through the successive hydrogenation of CO, i.e. CO + H → HCO + H → H_2CO + H → CH_2OH + H → CH_3OH (Tielens & Hagen 1982). Singly deuterated methanol is thought to form according to the same process, with one of the H atoms being replaced by deuterium while on the grain (Tielens 1983). In fact, these formation methods have been proven experimentally for both methanol (Watanabe & Kouchi 2002) and deuterated methanol (Watanabe et al. 2007).

Exactly how methanol and deuterated methanol enter the gas phase is still a matter of discussion. Proposed non-thermal mechanisms for COMs to leave ice mantles in cold, pre-stellar environments include UV-induced photodesorption, UV-induced codesorption, local heating or sputtering by cosmic rays, and reactive desorption, with each of these mechanisms facing varying degrees of theoretical and laboratory scrutiny (see Chuang et al. 2018, Pantaleone et al. 2020, and references therein). While the relative importance of these desorption mechanisms is still not known, observations of CH_2DOH in the gas phase through its millimetre-wavelength rotational transitions provide a link to studying deuteration on the icy surfaces of dust grains, and provide observational constraints on chemical models during the starless and pre-stellar core phases.

For this survey, we observed the complete population of starless and pre-stellar dense cores within a single region of a molecular cloud for the presence of singly deuterated methanol, CH_2DOH. In doing so, we look to understand the prevalence and abundance of the molecule in the incipient phases of star formation, as well as to explore deuterium fractionation within the surface ices of dust grains. This survey targeted low-mass (0.31–1.22 $M_\odot$) starless and pre-stellar dense cores in the Barnard 10 (B10) region of the Taurus molecular cloud, which were identified in the NH_3 mapping survey of Seo et al. (2015). The 12 starless and pre-stellar cores, Seo06–Seo17, contain the highest average abundance of methanol among the L1495–B218 regions (Scibelli & Shirley 2020). The B10 region has no embedded protostars (no Class 0/I/II protostars; Rebull et al. 2010) and is considered to be a less evolved, quiescent region free from stellar and protostellar activity (Hacar et al. 2013; Seo et al. 2015). Fig. 1 provides a map of these cores within the B10 region.

We present observations of CH_2DOH (Section 2) and calculate the deuterium fraction (Section 3) that is compared to models of grain surface deuteration as well as evolutionary indicators of the cores (Section 4).

2 OBSERVATIONS

Observations were taken with the Arizona Radio Observatory (ARO) 12-m Radio Telescope on Kitt Peak for 16 shifts between 2018 June and 2018 December towards the NH_3 peak positions (see Table 1) from Seo et al. (2015). We first tuned to the $J_{K_a,K_c} = 2_{0,2}$ e_0–$1_{0,1}$ e_0 (a-type) transition of CH_2DOH at 89.407817 GHz using the 3-mm receiver (ALMA mixers). Seo06 and 12 were observed in 2018 June using Millimeter AutoCorrelator (MAC) spectrometer. The observations have 0.0819 km s^{-1} (24.4 kHz) resolution and a full width at half-maximum (FWHM) beam size of 67.6 arcsec. We observed the remainder of the B10 region for the 89 GHz transition from 2018 October to 2018 November with the new

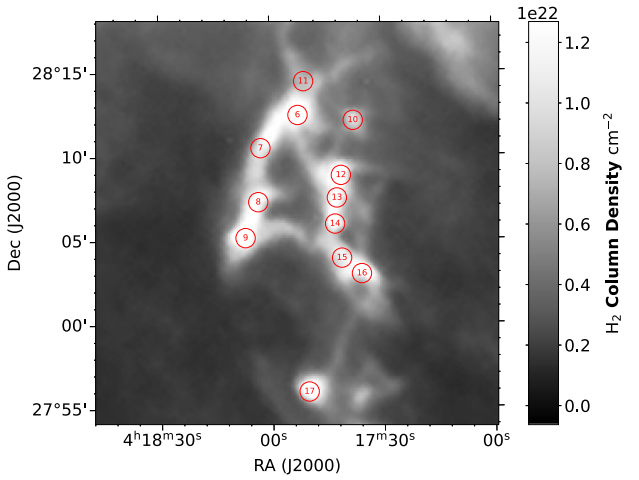

Figure 1. The B10 region of Taurus. The greyscale image is H_2 column density derived from *Herschel Space Observatory* observations (Palmeirim et al. 2013; Marsh et al. 2016). The positions of the NH_3-identifed cores (Seo et al. 2015) are indicated by the circles, which correspond to the beam size of the 12-m telescope.

Table 1. Source core numbers and coordinates are from Seo et al. 2015. Column density of methanol taken from Scibelli & Shirley 2020.

Core number	α (J2000.0)	δ (J2000.0)	N_{CH_3OH} (10^{13} cm^{-2})
6	4:17:52.8	+28:12:26	2.6 ± 0.1
7	4:18:02.6	+28:10:28	1.0 ± 0.1
8	4:18:03.7	+28:07:17	1.4 ± 0.1
9	4:18:07.0	+28:05:13	2.3 ± 0.1
10	4:17:37.6	+28:12:02	2.2 ± 0.1
11	4:17:51.2	+28:14:25	2.6 ± 0.1
12	4:17:41.7	+28:08:46	2.9 ± 0.1
13	4:17:42.2	+28:07:29	2.5 ± 0.1
14	4:17:43.0	+28:06:00	3.4 ± 0.2
15	4:17:41.1	+28:03:50	1.5 ± 0.1
16	4:17:36.1	+28:02:57	1.6 ± 0.1
17	4:17:50.3	+27:55:52	0.8 ± 0.1

AROWS spectrometer, which had become available in October. The AROWS spectrometer offered an improved resolution of 0.131 km s^{-1} (39 kHz). Additionally, we tuned with AROWS to the $J_{K_a,K_c} = 2_{1,1}$ e_0–$2_{0,2}$ e_0 (b-type) transition of CH_2DOH at 86.668751 GHz. We observed Seo09, 12, and 17 in this transition during three shifts between 2018 November and December.

Observations were conducted in one 8-h shift per source, with 5-min absolute position-switching scans between the source and off position every 30 s. The off position was the same position as used for NH_3 observations in Seo et al. (2015): $4^h18^m36.3^s$ $+28°5'43''.6$ J2000.0. Observed temperatures were converted from the antenna temperature scale T_A^* to the main beam temperature T_{mb} using measured beam efficiencies η_{mb} (Mangum 1993) correcting for the sideband rejection (typically better than 15 dB). Beam efficiencies were calculated from continuum observations of Mars, averaged over the two linear polarizations. These averaged beam efficiencies were $\eta_{mb} = 0.830 \pm 0.026$. There is an additional calibration ratio of 1.14 in T_A^* between newer AROWS spectrometer data and older MAC spectrometer data that was multiplied into all MAC observations. The average baseline RMS was $\sigma_{T_{mb}} = 11$ mK.

Table 2. CH_2DOH observations of starless and pre-stellar cores in B10. Spectra are analysed on the main beam temperature scale. All uncertainties for detected qunatities are 1σ. Non-detections for I and f_D values are reported as 3σ upper limits. ∗Seo06 and Seo12 are observed with a 0.0819 km s^{-1} resolution. All other cores have a resolution of 0.131 km s^{-1}.

Transition	Core number	v_{LSR} (km s^{-1})	Δv (km s^{-1})	I (mK km s^{-1})	N_{CH_2DOH} (10^{12} cm^{-2})	f_D
	6∗	6.43 ± 0.03	0.34 ± 0.07	11.8 ± 0.2	$1.0^{+0.4}_{-0.2}$	$0.04^{+0.02}_{-0.01}$
	7	6.45 ± 0.01	0.26 ± 0.03	15.9 ± 0.2	$1.3^{+0.5}_{-0.2}$	$0.14^{+0.06}_{-0.03}$
	8	6.54 ± 0.02	0.29 ± 0.04	23.3 ± 0.4	$2.0^{+0.8}_{-0.4}$	$0.14^{+0.07}_{-0.03}$
	9	6.62 ± 0.02	0.34 ± 0.04	33.7 ± 0.4	$2.9^{+1.0}_{-0.5}$	$0.13^{+0.05}_{-0.02}$
	10	5.32 ± 0.03	0.43 ± 0.07	29.2 ± 0.6	$2.5^{+1.1}_{-0.6}$	$0.11^{+0.06}_{-0.03}$
$2_{0,2}e_0$ - $1_{0,1}e_0$	11	...	...	<13.3	<1.4	<0.06
	12∗	5.56 ± 0.02	0.22 ± 0.04	19.2 ± 0.2	$1.6^{+0.5}_{-0.2}$	$0.06^{+0.02}_{-0.01}$
	13	...	...	<24.6	<2.5	<0.11
	14	...	...	<12.2	<1.3	<0.04
	15	6.54 ± 0.03	0.36 ± 0.07	18.5 ± 0.3	$1.6^{+0.7}_{-0.3}$	$0.11^{+0.06}_{-0.03}$
	16	6.48 ± 0.02	0.30 ± 0.05	14.8 ± 0.3	$1.3^{+0.6}_{-0.3}$	$0.08^{+0.04}_{-0.02}$
	17	6.72 ± 0.02	0.27 ± 0.05	22.3 ± 0.4	$1.9^{+0.8}_{-0.4}$	$0.23^{+0.12}_{-0.06}$
	9	6.77 ± 0.04	0.38 ± 0.08	10.4 ± 2.3	...	...
$2_{1,1}e_0$ - $2_{0,2}e_0$	12	5.58 ± 0.03	0.25 ± 0.09	7.2 ± 2.1	...	...
	17	6.73 ± 0.02	0.23 ± 0.04	17.3 ± 8.5	...	...

Sources in the B10 regions are at an average distance of 135 pc (Schlafly et al. 2014) with an average angular size of about 1 arcmin that is well matched to our resolution. The FWHM beam size of 67 arcsec at this distance corresponds to 0.044 pc.

3 DATA REDUCTION AND ANALYSIS

CH_2DOH was detected in 9 of the 12 observed cores with greater than $3\sigma_{T_{mb}}$ certainty. Non-detections were taken to have an intensity upper limit of three times the integrated intensity *rms*, which averaged $3\sigma_1 = 0.017$ K km s^{-1}. These data were reduced using the CLASS program of the GILDAS package,[1] with which Gaussian line profiles were fit to the spectra to calculate integrated intensity, velocity, and FWHM linewidth (see Table 2) using standard CLASS routines (Pety 2005, Gildas Team 2013). The symmetric, Gaussian shapes of the spectra were well fit by a single Gaussian profile (Fig. 2). All CH_2DOH linewidths are narrower than the corresponding CH_3OH linewidth with a median linewidth ratio of 0.78 (Table 2).

The deuterium fraction, $f_D = N(CH_2DOH)/N(CH_3OH)$, of methanol in the cores is calculated by deriving the column density of CH_2DOH and dividing by the total column density (adding A + E symmetry states) of CH_3OH previously published by Scibelli & Shirley (2020). CH_3OH column densities (see Table 1) were determined using the 1D non-LTE RADEX code (van der Tak et al. 2007). Three transitions of CH_3OH were modelled assuming the core was characterized by a homogeneous average density derived from *Herschel* continuum observations (Palmeirim et al. 2013; Marsh et al. 2016) and an isothermal gas kinetic temperature derived from NH_3 observations (Seo et al. 2015) with no large-scale velocity motions (see Scibelli & Shirley (2020) for details). Since there are no published collision rates for CH_2DOH, we cannot use RADEX to estimate column densities for the deuterated species. Instead, the column density of CH_2DOH (cm^{-2}) is determined from

$$N(CH_2DOH) = \frac{4\pi}{hcg_uA_{ul}} \frac{B_\nu(T_{ex})Q(T_{ex})e^{E_u/kT_{ex}}}{[J_\nu(T_{ex}) - J_\nu(T_{cmb})]} I(CH_2DOH), \quad (1)$$

where A_{ul} is the spontaneous emission coefficient of the CH_2DOH transition at frequency ν, E_u, and g_u are the upper level energy and statistical weight, T_{ex} is the excitation temperature of the CH_2DOH transition, Q is the partition function, $I(CH_2DOH)$ is the integrated intensity of the line (K cm s^{-1}), and B_ν and J_ν are *Planck* functions in intensity and temperature units, respectively (see Mangum & Shirley 2015 for a derivation). For the 89-GHz a-type transition, we assumed values derived from the JPL line catalogue entry[2] of $A_{ul} = 2.02 \times 10^{-6}$ s^{-1}, $gu = 5$, and $E_u/k = 6.44$ K (Pickett et al. 1998). For the 86-GHz b-type transition, we used $A_{ul} = 4.65 \times 10^{-6}$ s^{-1}, $gu = 5$, and $E_u/k = 10.60$ K. This equation assumes that the CH_2DOH emission is optically thin, that the filling fraction of emission is equal to 1, and that all of the rotational energy levels are populated with the same excitation temperature (the CTEX or constant excitation temperature approximation; Caselli et al. 2002b; Mangum & Shirley 2015). Given the different energy level structure of CH_2DOH compared to CH_3OH, it is likely that the CH_2DOH excitation temperature is different than the excitation temperatures calculated by RADEX for CH_3OH transitions.

Typically, observations of two optically thin transitions with different E_u/k at similar spatial resolutions may be used to simultaneously constrain the total column density and excitation temperature in the CTEX approximation; however, the uncertainty associated with calculating the matrix elements for b-type and c-type transitions of CH_2DOH presents a challenge with our observations (see Appendix A). We attempted to overlay the column density versus T_{ex} curves using the same procedure outlined in Scibelli & Shirley (2020) for the three sources for which two CH_2DOH transitions were observed in this survey, but the curves did not overlap for $T_{ex} > T_{cmb}$ (Fig. 3). This either indicates that there is significant non-LTE

[1] https://www.iram.fr/IRAMFR/GILDAS/

[2] https://spec.jpl.nasa.gov/ftp/pub/catalog/c033004.cat

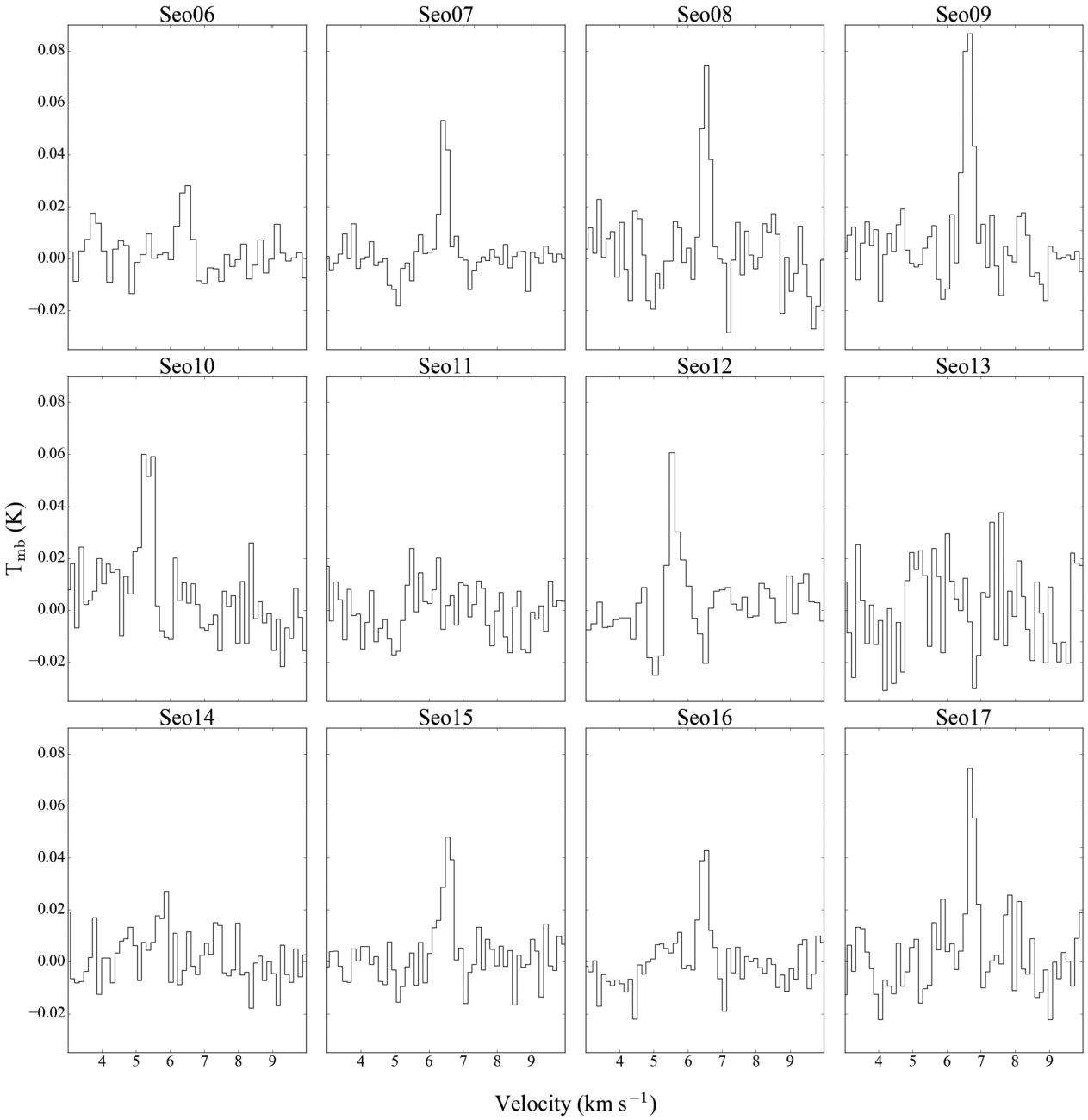

Figure 2. Spectra of all observed sources for the 89 GHz $2_{0,2}$ e_0–$1_{0,1}$ e_0 (a-type) transition of CH_2DOH. Detection peaks can be seen for all sources except Seo 11, 13, and 14. The velocity scale is radio v_{LSR}.

excitation occurring for the CH_2DOH transitions (with population inversions) in pre-stellar cores or that we do not have an accurate value for the Einstein A of the b-type transition to make a reasonable estimate of T_{ex} using this method (see Appendix A).

Since a reliable single value for the CH_2DOH T_{ex} could not be calculated from the two observed transitions, the column densities of CH_2DOH were calculated for a range of possible excitation temperatures using only the a-type transition. These column densities were divided by the total CH_3OH column densities (adding A + E symmetry states) measured for the cores (Scibelli & Shirley 2020) to obtain values of f_D. A plot of f_D versus T_{ex} of CH_2DOH for each detected source shows that the resultant curves increase for $T_{ex} < 4$ K, and climb again for $T_{ex} > 8$ K (Fig. 3). Between these values, however, f_D is relatively flat. As f_D is slightly higher for all sources at $T_{ex} = 4$ K than $T_{ex} = 8$ K, we took 4 K as our excitation temperature lower limit, and therefore as an upper limit on the column density of CH_2DOH and f_D for each source. Admittedly, this exact choice is arbitrary; however, the CH_3OH excitation temperatures of these sources typically range from ∼7–8 K (Scibelli & Shirley 2020). Given the large deuteration values we find below, it therefore seems unlikely that CH_2DOH has excitation temperatures much below 4 K. The curves for all sources reach a minimum f_D at $T_{ex} = 5.6$ K, and we took that T_{ex} value for the column density of CH_2DOH and f_D lower limits. We took the

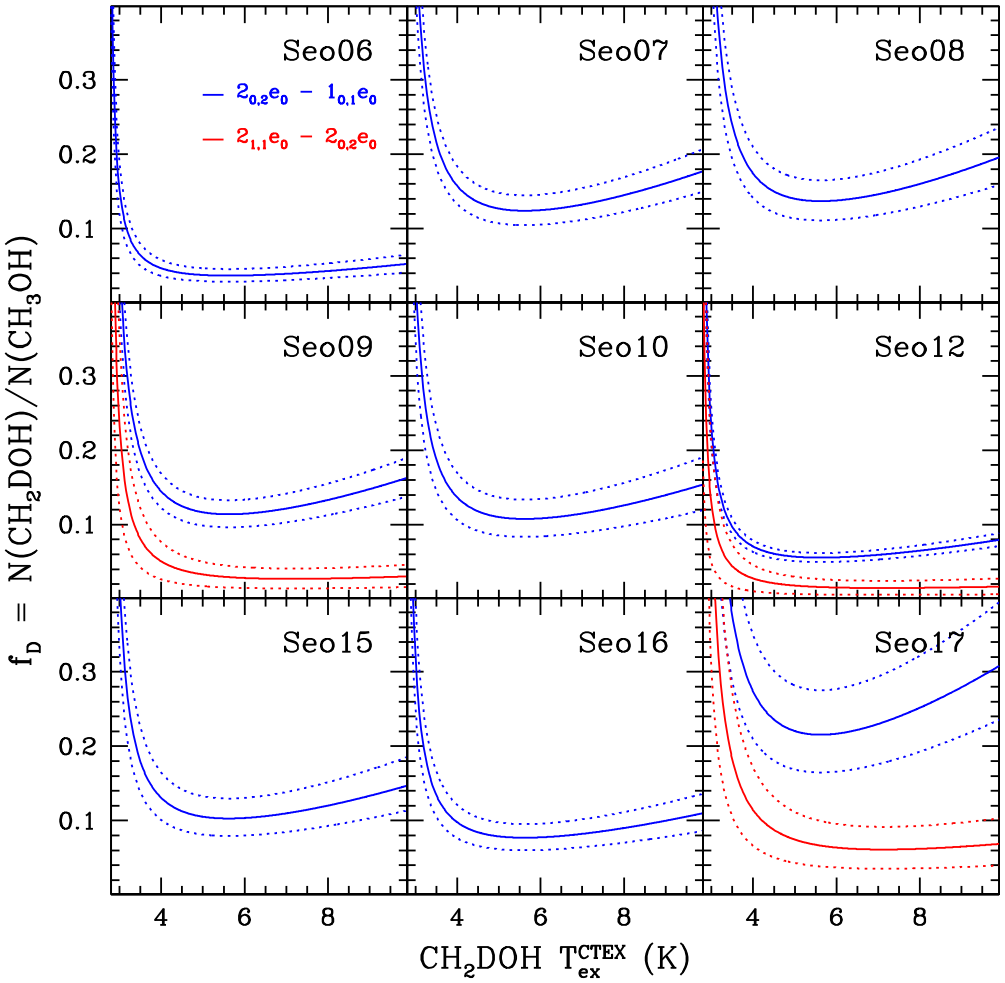

Figure 3. The deuterium fraction $f_D = N(CH_2DOH)/N(CH_3OH)$ is plotted for the detected sources versus the excitation temperature (CTEX approximation) of the CH_2DOH transition. The blue curves correspond to the a-type $2_{0,2}e_0$–$1_{0,1}e_0$ transition, and the red curves correspond to the b-type $2_{1,1}e_0$–$2_{0,2}e_0$ transition. The solid line is f_D, while the dashed lines are $\pm1\sigma$.

median values between the lower and upper limits described to estimate the column density of CH_2DOH and f_D for each core. f_D was found to range between 0.04 and 0.23 for the detected sources (Table 2).

4 DISCUSSION

4.1 Comparison with chemical models

Our observed abundance ratios are consistent with observations of L1544, which showed a deuterium fractionation of methanol of $f_D = 0.08 \pm 0.02$ (Chacón-Tanarro et al. 2017, 2019). Because f_D does not vary strongly with T_{ex} within the range 4–8 K (typically 20 per cent), our method of choosing T_{ex} for this paper is consistent with the methods used by Bizzocchi et al. (2014) and Chacón-Tanarro et al. (2019) to estimate the excitation temperature of singly deuterated methanol. Since observations are limited to gas-phase molecules, the abundance on the grain surfaces is unknown. Therefore, we must compare our observations to predictions of gas-grain chemical models.

Methanol is predicted to be deuterated on the icy grain surfaces either by the addition of atomic D to CO, by deuterium-substitution reactions with methanol, or by a combination of the two (Tielens 1983; Charnley, Tielens & Rodgers 1997; Taquet, Ceccarelli & Kahane 2012b). The first process requires CO freeze-out to begin, as well as high atomic D/H ratios (Caselli et al. 2002a; Parise et al. 2006). Large gas phase atomic D/H ratios (>0.1) are predicted in regions where significant CO freeze-out has occurred as a result of the dissociative recombination of fractionated H_2D^+, D_2H^+, and D_3^+ (Roberts et al. 2003). Indeed, the D/H ratio has been measured to increase in pre-stellar cores for higher CO depletion, and thus higher density (Bacmann et al. 2002, 2003; Crapsi et al. 2005). The process of methanol deuteration via deuterium-substitution reactions has been measured in the laboratory and can reproduce large deuterium fractions (Nagaoka, Watanabe & Kouchi 2005).

Taquet et al. (2012b) analysed the deuteration of methanol on the dust grains of late-stage, low-mass pre-stellar cores using the GRAINOBLE model introduced in Taquet, Ceccarelli & Kahane 2012a. GRAINOBLE is a time-dependent gas-grain chemical model that relies on the rate equations method, differing from previous models by treating the grain as a reactive outer layer surrounding an inert mantle bulk (Hasegawa & Herbst 1993; Garrod & Pauly 2011) while including both H and D addition to atomic CO and H/D substitution reactions, and allowing the H/D ratio to vary throughout

the simulation (Caselli et al. 2002a; Stantcheva & Herbst 2003). The model finds that for $n_H = 10^5$ cm^{-3}, similar to the average density of cores dervied by Scibelli & Shirley (2020), the mean f_D = [CH_2DOH]/[CH_3OH] in the ice reaches values ranging from 0.05–0.16 by t = 10^6 yr. These model estimates agree with the median values of f_D observed in the gas phase towards the B10 region for all cores detected in methanol with the exception of Seo17, whose lower limit value ($f_D = 0.165$) is just above the model range. This would indicate, if the model predictions are accurate, that a significant fraction of the CH_2DOH formed in the ices at densities of 10^5 cm^{-3} desorbes into the gas phase.

For higher density values ($\sim 5 \times 10^6$ cm^{-3}), which will occur as the pre-stellar core evolves towards a first hydrostatic core, the Taquet et al. (2012b) models predict even higher ice deuterium fractions. This should be observable during the initial stages of protostellar accretion as heating desorbs the ice mantles. Single-dish observations out to ∼1000 au by Parise et al. (2002, 2004, 2006) indeed show higher deuterium fractions (∼0.3–0.6) for methanol in Class 0 protostars. Ultimately, the deuterium fraction of methanol is predicted to decrease towards the warm central regions (<100 au) of the core envelope as the protostar evolves (Taquet, Charnley & Sipilä 2014), which has been confirmed by recent interferometric observations of Class 0/I protostars (Bianchi et al. 2017a,b; Jørgensen et al. 2018; Persson et al. 2018; Taquet et al. 2019; Manigand et al. 2020; van Gelder et al. 2020).

4.2 Evolutionary comparisons

Deuterium fractionation has traditionally been used as a chemical evolutionary indicator towards starless and pre-stellar cores (Crapsi et al. 2005). Some molecules, such as NH_3 or N_2H^+, are considered 'late-time' species since their abundances tend to peak during more advanced stages of starless core evolution. In constrast, CH_3OH is considered an 'early-time' species since its abundance peaks early in the core's evolution when CO begins to deplete on to dust grains, after which its abundance decreases as CH_3OH itself freezes out of the gas phase in the central dense, cold regions. CH_2DOH is a probe of deuterium fractionation in an 'early-time' species; however, there is difficulty in assigning CH_2DOH as an 'early-time' species since deuterium fraction tends to increase during starless core evolution. There is also difficulty in assigning CH_2DOH as a 'late-time' species, as maps of L1544 indicate that emission from this molecule does not peak at the dust continuum peak as other 'late-time' species do (Chacón-Tanarro et al. 2019). With this tension in mind, we have investigated how the methanol deuterium fraction varies with evolutionary parameters of the cores (Fig. 4).

As a starless core evolves to a pre-stellar core and eventually to a first hydrostatic core, the central density of the core increases and the core becomes more gravitationally bound. The virial ratio is one metric for determining the evolutionary stage of starless cores. The virial ratio α is defined as the ratio of twice the total kinetic energy to the total gravitational potential, $\alpha = |\frac{2\Omega}{\Omega}\frac{K}{G}|$. Since starless cores have density profiles that tend to be flat towards the centre and then fall off like a power law (i.e. Bonnor-Ebert spheres or Plummer-like spheres; Ebert 1955; Bonnor 1956; Whitworth & Ward-Thompson 2001) and since the change of the numerical coefficient in the gravitational potential energy term between a uniform density sphere and a critical Bonnor–Ebert sphere is only 0.6–0.73, respectively (Sipilä, Harju & Juvela 2011), we shall simply assume the coefficient for a uniform density core and therefore $\alpha = 5R\sigma_v^2/GM$. Larger values of α indicate less gravitationally-bound objects and smaller values indicate more gravitationally-bound (and presumably more evolved)

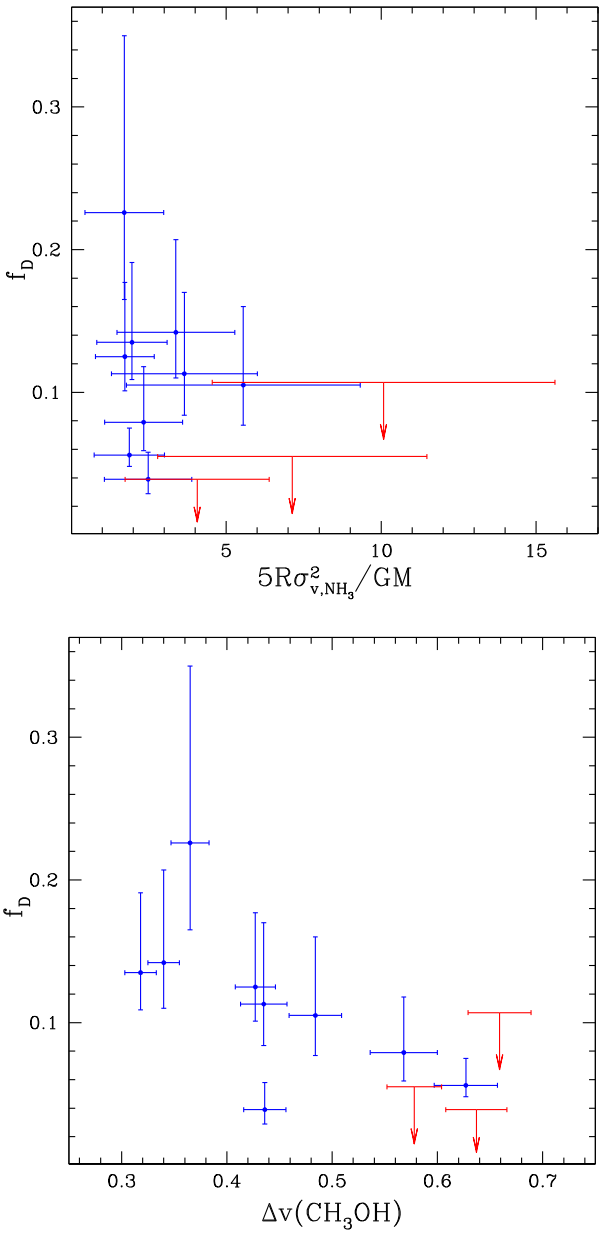

Figure 4. (Top) A plot of deuterium fraction f_D = N(CH_2DOH)/N(CH_3OH) versus the virial ratio $\alpha = |\frac{2\Omega}{\Omega}\frac{K}{U}|$ and (Bottom) linewidth, Δv, of CH_3OH-A $J_K = 2_0 - 1_0$ for the starless cores of the B10 region. Sources detected in CH_2DOH are shown in blue, while non-detections are shown in red with 3σ upper limits.

objects. We note that this simple virial ratio ignores potentially important contributions from the external pressure, internal magentic fields, and any mass flow across the core boundary; however, it simply provides a quick estimate of the importance of gravitational potential energy to the internal kinetic energy. Virial ratios for the cores in the survey were reported in Scibelli & Shirley (2020) and were calculated using the size of the NH_3 core dendrogram, the NH_3 (1,1) velocity dispersion (Seo et al. 2015), and the mass within the core dendrogram boundary determined from the *Herschel*-derived N(H_2) map of Palmeirim et al. (2013). The uncertainty on the dendrogram-derived core size is assumed to be one half of a pixel around the boundary. Error bars on the virial ratio are statistical and do not include systematic uncertainties, for instance, in the assumed dust

opacities (Shirley et al. 2005, 2011; Howard et al. 2019). A plot of f_D versus α (Fig. 4) shows that cores not detected in CH_2DOH tend to have higher virial ratios ($\alpha > 4$), although the statistical error bars on the virial ratio are substantial. This result is consistent with CH_2DOH non-detections towards less-evolved starless cores. There also is no significant correlation between CH_3OH deuterium fraction and the virial parameter.

The most robust trend (Pearson correlation coefficient of -0.63 and rank correlation coefficent of -0.82) is that the deuterium fractionation is anticorrelated with the FWHM linewidth of the CH_3OH molecule (Fig. 4). The FWHM linewidth is a result of the gas motions within the telescope beam, with more turbulent sources exhibiting larger non-thermal doppler motions, and therefore larger linewidths. We note that CH_3OH is not exclusively a dense core tracer, as extended CH_3OH emission is seen in the lower density filamentary structure in which the starless cores are embedded (Scibelli & Shirley 2020). Since the turbulent motions of starless cores dissipate as the cores evolve, the linewidths of their spectra decreases with age. Three of the four starless cores with the largest linewidths are non-detections in CH_2DOH. The ratio of the linewidths of non-detections to the linewidths of detections is 1.4. This result is consistent with the conclusion that higher deuterium fraction is associated with more-evolved cores.

5 CONCLUSIONS

Observations of 12 starless and pre-stellar cores in the B10 region of the Taurus molecular cloud show the presence of gas phase singly deuterated methanol, CH_2DOH, in 75 per cent of its starless and pre-stellar dense cores. All CH_2DOH FWHM linewidths are narrower than the corresponding CH_3OH linewidths with a median ratio of 0.78. The deuterium fraction of CH_2DOH to its non-deuterated form, CH_3OH, ranges from <0.04 to $0.23^{+0.12}_{-0.06}$ with a median value of 0.11. These values are consistent with previous observations of the pre-stellar dense core L1544, also in Taurus, as well as with the theoretical values derived in the Taquet et al. (2012b) ice chemistry model. The cores detected in CH_2DOH appear to be more evolved, on average, than their non-detected counterparts (which have larger virial parameters and larger CH_3OH linewidth than detected cores), though the region as a whole is relatively young compared to other regions within the Taurus molecular cloud. This survey indicates that deuterium fractionation in organic molecules such as CH_3OH may be more easily detectable than previously thought and, in the case of CH_2DOH, may provide a probe of the deuteration on the icy surfaces of dust grains from molecules that are desorbed into the gas phase. Our observations provide new constraints for gas-grain astrochemical models of starless and pre-stellar cores that are more representative of a typical core than some of the more extreme objects studied to date.

ACKNOWLEDGEMENTS

We sincerely thank the referee for their comments that improved this paper. We also sincerely thank the staff and the operators of the Arizona Radio Observatory (Michael Begam, Kevin Bays, Robert Thompson, and Clayton Kyle) for their assistance with the observations. We are thankful that we have the opportunity to conduct astronomical research on Iolkam Du'ag within the Tohono O'odham Nation. Hannah Ambrose, Yancy Shirley, and Samantha Scibelli were supported by a National Science Foundation Astronomy and Astrophysics Grant AST-1410190 (PI Shirley). Samantha Scibelli is also supported by a National Science Foundation Graduate Research Fellowship (NSF GRF) grant DGE-1143953. The 12-m Telescope is operated by the Arizona Radio Observatory, Steward Observatory, University of Arizona, with funding from the State of Arizona, National Science Foundation Major Research Intrumentation Program grant AST-1531366 (PI Ziurys), National Science Foundation Mid-Scale Innovaitons Program in Astronomical Sciences grant SV5-85009/AST- 1440254 (PI Marrone), National Science Foundation Faculty Early Career Development Program grant AST-1653228 (PI Marrone), and an National Science Foundation Partnerships for International Research and Education grant OISE-1743747 (PI Psaltis).

DATA AVAILABILITY

The data underlying this article will be shared on reasonable request to the corresponding authors.

REFERENCES

André P., Di Francesco J., Ward-Thompson D., Inutsuka S. I., Pudritz R. E., Pineda J. E., 2014, in Beuther H., Klessen R. S., Dullemond C. P., Henning T., eds, Protostars and Planets VI, Univ. Arizona Press, Tucson, AZ, p. 27
Bacmann A., Lefloch B., Ceccarelli C., Castets A., Steinacker J., Loinard L., 2002, A&A, 389, L6
Bacmann A., Lefloch B., Ceccarelli C., Steinacker J., Castets A., Loinard L., 2003, ApJ, 585, L55
Bacmann A., Taquet V., Faure A., Kahane C., Ceccarelli C., 2012, A&A, 541, L12
Benson P. J., Myers P. C., 1989, ApJS, 71, 89
Bergin E. A., Tafalla M., 2007, ARA&A, 45, 339
Bianchi E. et al., 2017a, MNRAS, 467, 3011
Bianchi E. et al., 2017b, A&A, 606, L7
Bizzocchi L., Caselli P., Spezzano S., Leonardo E., 2014, A&A, 569, A27
Bonnor W. B., 1956, MNRAS, 116, 351
Caselli P., Sipilä O., Harju J., 2019, Phil. Trans. R. Soc. A, 377, 20180401
Caselli P., Stantcheva T., Shalabiea O., Shematovich V. I., Herbst E., 2002a, Planet. Space Sci., 50, 1257
Caselli P., Walmsley C. M., Zucconi A., Tafalla M., Dore L., Myers P. C., 2002b, ApJ, 565, 344
Ceccarelli C., Caselli P., Bockelée-Morvan D., Mousis O., Pizzarello S., Robert F., Semenov D., 2014, in Beuther H., Klessen R. S., Dullemond C. P., Henning T., eds, Protostars and Planets VI. Univ. Arizona Press, Tucson, AZ, p. 859
Chacón-Tanarro A., Caselli P., Bizzocchi L., Pineda J. E., Spezzano S., Giuliano B. M., Lattanzi V., Punanova A., 2017, Mem. Soc. Astron. Italiana, 88, 724
Chacón-Tanarro A. et al., 2019, A&A, 622, A141
Charnley S. B., Tielens A. G. G. M., Rodgers S. D., 1997, ApJ, 482, L203
Chuang K.-J., Fedoseev G., Qasim D., Ioppolo S., van Dishoeck E. F., Linnartz H., 2018, ApJ, 853, 102
Cooke R. J., Pettini M., Nollett K. M., Jorgenson R., 2016, ApJ, 830, 148
Crapsi A., Caselli P., Walmsley C. M., Myers P. C., Tafalla M., Lee C. W., Bourke T. L., 2005, ApJ, 619, 379
di Francesco J., Evans N. J. I., Caselli P., Myers P. C., Shirley Y., Aikawa Y., Tafalla M., 2007, in Reipurth B., Jewitt D., Keil K., eds, Protostars and Planets V. Univ. Arizona Press, Tucson, AZ, p. 17
Ebert R., 1955, Z. Astrophys., 37, 217
Epstein R. I., Lattimer J. M., Schramm D. N., 1976, Nature, 263, 198
Evans N. J. I., Rawlings J. M. C., Shirley Y. L., Mundy L. G., 2001, ApJ, 557, 193
Garrod R. T., Pauly T., 2011, ApJ, 735, 15
Geppert W. D. et al., 2006, Faraday Discuss., 133, 177

Gildas Team, 2013, Astrophysics Source Code Library, record ascl:1305.010
Hacar A., Tafalla M., Kauffmann J., Kovács A., 2013, A&A, 554, A55
Hasegawa T. I., Herbst E., 1993, MNRAS, 263, 589
Herbst E., van Dishoeck E. F., 2009, ARA&A, 47, 427
Howard A. D. P., Whitworth A. P., Marsh K. A., Clarke S. D., Griffin M. J., Smith M. W. L., Lomax O. D., 2019, MNRAS, 489, 962
Jiménez-Serra I. et al., 2016, ApJ, 830, L6
Jørgensen J. K. et al., 2018, A&A, 620, A170
Loinard L. et al., 2002, Planet. Space Sci., 50, 1205
Mangum J. G., 1993, PASP, 105, 117
Mangum J. G., Shirley Y. L., 2015, PASP, 127, 266
Manigand S. et al., 2019, A&A, 623, A69
Manigand S. et al., 2020, A&A, 635, A48
Marsh K. A. et al., 2016, MNRAS, 459, 342
Millar T. J., Bennett A., Herbst E., 1989, ApJ, 340, 906
Mukhopadhyay I., 2016, Infrared Phys. Technol., 77, 283
Mukhopadhyay I., Billinghurst B. E., 2016, Infrared Phys. Technol., 79, 216
Nagaoka A., Watanabe N., Kouchi A., 2005, ApJ, 624, L29
Palmeirim P. et al., 2013, A&A, 550, A38
Pantaleone S., Enrique-Romero J., Ceccarelli C., Ugliengo P., Balucani N., Rimola A., 2020, ApJ, 897, 56
Parise B., Castets A., Herbst E., Caux E., Ceccarelli C., Mukhopadhyay I., Tielens A. G. G. M., 2004, A&A, 416, 159
Parise B., Ceccarelli C., Tielens A. G. G. M., Castets A., Caux E., Lefloch B., Maret S., 2006, A&A, 453, 949
Parise B. et al., 2002, A&A, 393, L49
Pearson J. C., Yu S., Drouin B. J., 2012, J. Mol. Spectrosc., 280, 119
Persson M. V. et al., 2018, A&A, 610, A54
Pety J., 2005, in Casoli F., Contini T., Hameury J. M., Pagani L., eds, SF2A-2005: Semaine de l'Astrophysique Francaise, EdP-Sciences, Les Ulis, France. p. 721
Pickett H. M., Poynter R. L., Cohen E. A., Delitsky M. L., 1998, Journal of Quantitative Spectroscopy and Radiative Transfer, 60, 885
Planck Collaboration XIII, 2016, A&A, 594, A13
Rebull L. M. et al., 2010, ApJS, 186, 259
Roberts H., Herbst E., Millar T. J., 2003, ApJ, 591, L41
Schlafly E. F. et al., 2014, ApJ, 786, 29
Scibelli S., Shirley Y., 2020, ApJ, 891, 73
Seo Y. M. et al., 2015, ApJ, 805, 185
Shirley Y. L., Huard T. L., Pontoppidan K. M., Wilner D. J., Stutz A. M., Bieging J. H., Evans N. J. I., 2011, ApJ, 728, 143
Shirley Y. L., Nordhaus M. K., Grcevich J. M., Evans N. J. I., Rawlings J. M. C., Tatematsu K., 2005, ApJ, 632, 982
Sipilä O., Harju J., Juvela M., 2011, A&A, 535, A49
Soma T., Sakai N., Watanabe Y., Yamamoto S., 2018, ApJ, 854, 116
Stantcheva T., Herbst E., 2003, MNRAS, 340, 983
Tafalla M., 2016, in Jablonka P., André P., van der Tak F., eds, Proc. IAU Symp. 315, From Interstellar Clouds to Star-Forming Galaxies: Universal Processes? Kluwer, Dordrecht, p. 95
Taquet V., Ceccarelli C., Kahane C., 2012a, A&A, 538, A42
Taquet V., Ceccarelli C., Kahane C., 2012b, ApJ, 748, L3
Taquet V., Charnley S. B., Sipilä O., 2014, ApJ, 791, 1
Taquet V. et al., 2019, A&A, 632, A19
Tielens A. G. G. M., 1983, A&A, 119, 177
Tielens A. G. G. M., Hagen W., 1982, A&A, 114, 245
van der Tak F. F. S., Black J. H., Schöier F. L., Jansen D. J., van Dishoeck E. F., 2007, A&A, 468, 627
van Gelder M. L. et al., 2020, A&A, 639, A87
Watanabe N., Hidaka H., Nagaoka A., Kouchi A., 2007, in Lemaire J.-L., Combes F., eds, Molecules in Space and Laboratory, Observatoire de Paris, Paris, France. p. 52
Watanabe N., Kouchi A., 2002, ApJ, 571, L173
Whitworth A. P., Ward-Thompson D., 2001, ApJ, 547, 317

APPENDIX A: ROTATIONAL TRANSITIONS OF SINGLY DEUTERATED METHANOL

CH_2DOH is an asymmetric top molecule with torsional motions that has allowed a-type transitions ($\Delta K_a = 0, \pm2, \ldots, \Delta K_c = \pm1, \pm3, \ldots$), b-type transitions ($\Delta K_a = \pm1, \pm3, \ldots, \Delta K_c = \pm1, \pm3, \ldots$), and c-type transitions ($\Delta K_a = \pm1, \pm3, \ldots, \Delta K_c = 0, \pm2, \ldots$). The lowest rotational energy levels are shown in Fig. A1. The methyl-D_1 (CH_2D) group is an example of an asymmetric hindered rotor in the CH_2DOH molecule (Pearson, Yu & Drouin 2012; Mukhopadhyay 2016; Mukhopadhyay & Billinghurst 2016) that results in three energetically separated torsional symmetry substates (even or odd functions of the torsional angle) for each ground state asymmetric top rotational level (J_{K_a,K_c}) that are labelled as e_0 (trans), e_1 (gauche), and o_1 (gauche). Since the molecular a-axis component of the dipole moment is independent of the torsional angle, a-type transitions are only permitted within the same torsional symmetry substate (i.e. $e_0 \rightarrow e_0$) and their matrix elements are more precisely calculated. For b-type transitions, the torsional substate selection rules are more complicated and can change substates while maintaining torsional substate parity (i.e. $e_0 \rightarrow e_0$, $e_1 \rightarrow e_1$, $e_0 \leftrightarrow e_1$, and $o_1 \rightarrow o_1$ allowed). c-type transitions cross torsional substates with different symmetry (i.e. $e_0 \leftrightarrow o_1$ allowed). The matrix elements for b-type and c-type transitions are more uncertain than for a-type transitions as they involve the mutliplication of the torsional overlap integral (a function of torsional excitation, substate and symmetric top K value, which is a strong function of J) times the rotational dipole matrix element, and the b and c dipoles have significant three-fold sine and cosine terms that are unknown (J. Pearson 2019, private communication). The JPL line catalog entry for CH_2DOH has a dire warning to use extreme caution when determining column densities from b-type and c-type transitions.[3] Our analysis in this paper confirms this warning.

[3] https://spec.jpl.nasa.gov/ftp/pub/catalog/doc/d033004.pdf

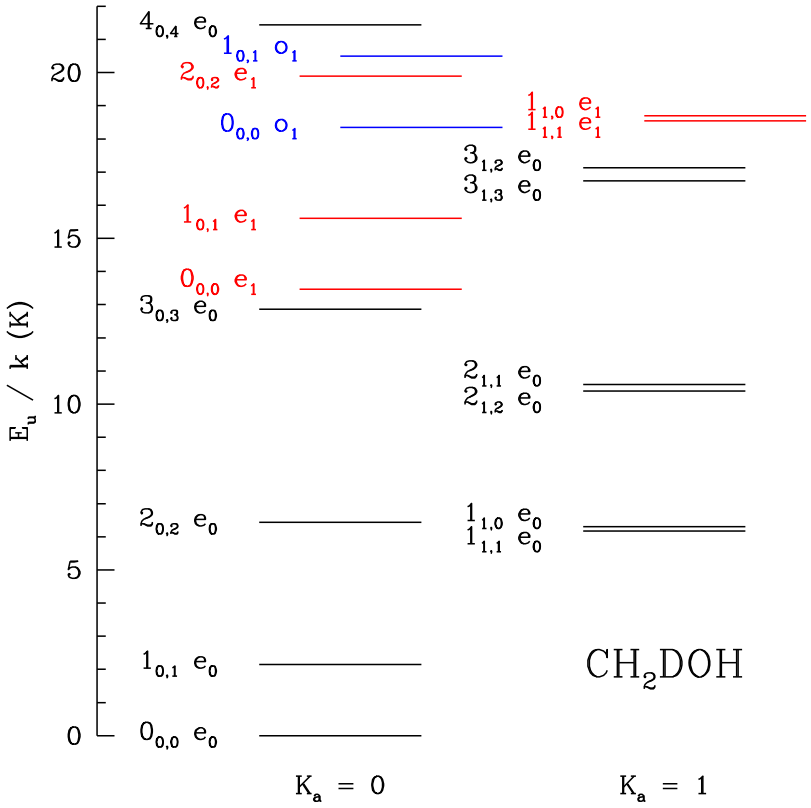

Figure A1. Energy level diagram for bound states of CH_2DOH with $E_u/k < 22$ K. Different torsional symmetry substates are plotted as slightly offset within each K_a ladder and colour coded as e_0 (black), e_1 (red), and o_1 (blue). Each torsional symmetry substate follows the same general pattern of asymmetric top rotational energy levels but offset in energy from each other. Note that the lowest energy level with $K_a = 2$ is the $2_{2,1}$ e_0 level with $E_u/k = 22.6$ K.

This paper has been typeset from a TEX/LATEX file prepared by the author.